Weak ferromagnetism in hexagonal Mn₃Z alloys (Z = Sn, Ge, Ga)

B. Nyári ⬤, A. Deák ⬤, and L. Szunyogh

Department of Theoretical Physics, Budapest University of Technology and Economics, Budafoki út 8., HU-1111 Budapest, Hungary
and MTA-BME Condensed Matter Research Group, Budapest University of Technology and Economics,
Budafoki út 8., HU-1111 Budapest, Hungary

We present combined spin model and first-principles electronic-structure calculations to study the weak ferromagnetism in bulk Mn_3Z (Z = Sn, Ge, Ga) compounds. The spin-model parameters were determined from a spin-cluster expansion technique based on the relativistic disordered local moment formalism implemented in the screened Korringa–Kohn–Rostoker method. We describe the magnetic ground state of the system within a three-sublattice model and investigate the formation of the weak ferromagnetic states in terms of the relevant model parameters. First, we give a group-theoretical argument how the point-group symmetry of the lattice leads to the formation of weak ferromagnetic states. Then we study the ground states of the classical spin model and derive analytical expressions for the weak ferromagnetic distortions by recovering the main results of the group-theoretical analysis. As a third approach, we obtain the weak ferromagnetic ground states from self-consistent density-functional calculations and compare our results with previous first-principles calculations and with available experimental data. In particular, we demonstrate that the orbital moments follow a decomposition predicted by group theory. For a deeper understanding of the formation of weak ferromagnetism, we selectively trace the effect of the spin-orbit coupling at the Mn and Z sites. In addition, for the case of Mn_3Ga, we gain information on the role of the induced moment of Ga from constrained local density-functional calculations.

I. INTRODUCTION

The Mn_3Z (Z= Sn, Ge, Ga) compounds, known to be weak ferromagnetic (WF) at low temperatures [1–3], are in the focus of current research interest due to the exotic topological properties of their band structure. They show large anomalous Hall conductivity due to the nonvanishing Berry curvature induced by the noncollinear triangular ground-state spin structure [4–6] and are topological Weyl semimetals because of emerging Weyl nodes in the band structure near the Fermi level [7,8]. The Mn_3Z compounds are also possible candidates to replace the expensive IrMn-based antiferromagnets in magnetic sensors based on the GMR effect [9].

The Mn_3Z compounds have three different structural phases: a hexagonal phase with DO_{19} structure, a tetragonal phase with DO_{22} structure, and a cubic phase with a standard Heusler structure. These phases and the transitions between them have been the subject of recent research [10,11]. In this paper, we are going to investigate the magnetic properties in the hexagonal phase of these compounds. The atomic positions in the DO_{19} hexagonal phase are sketched in Fig. 1. The Mn sites in each layer form a kagome lattice, i.e., a two-dimensional network of corner-sharing equilateral triangles. The atomic layers are shifted alternately with $\frac{2}{3}(\vec{a} + \vec{b})$ and $\frac{1}{3}(\vec{a} + \vec{b})$, where $\vec{a}$ and $\vec{b}$ are the primitive vectors of the kagome lattice. The unit cell marked by the black rhombus in Fig. 1 contains two layers built up from six manganese atoms and two nonmagnetic Z atoms.

The magnetic structure of these materials was measured with polarized neutron-diffraction experiments showing that the low-energy magnetic states of these compounds in the

hexagonal phase are chiral antiferromagnetic (AFM) states [1–3] as illustrated in Fig. 2, with a small distortion producing a tiny net magnetic moment. A simple spin-model analysis in Ref. [1] proved the magnetocrystalline anisotropy to be the microscopic mechanism responsible for the WF distortion, whereas the Dzyaloshinsky–Moriya (DM) interaction [12,13] was shown to lift the chiral degeneracy of the Γ_3 and Γ_5 states.

The electronic and magnetic structure of these compounds was also investigated theoretically in terms of self-consistent field density-functional calculations in the local density approximation (LDA) [4,10,11,14,15]. In the hexagonal phase, the chiral Γ_5 state with a WF distortion and a small net magnetic moment was found as ground state [4,10,15]. In particular, Ref. [15] discussed symmetry considerations and the role of orbital polarization on the formation of weak ferromagnetism in Mn_3Sn. It should be noted that in Ref. [10] the tetragonal phase of Mn_3Sn was found lower in energy than the hexagonal phase and the stability of the hexagonal phase according to experiments was attributed to structural disorder or off-stoichiometric compositions. The influence of these effects on the magnetic ordering in the Mn_3Ga alloy has been studied in Ref. [11].

In this paper, we present a detailed theoretical investigation of the magnetic ground state of the Mn_3Z alloys in the hexagonal phase. We employ the relativistic Screened Korringa–Kohn–Rostoker (SKKR) method [16,17] to calculate the electronic structure and the magnetic properties. In particular, we set up a classical spin model with parameters obtained from the combination of the spin-cluster expansion (SCE) and the relativistic disordered local moment (RDLM) method [18]. Using the point-group symmetry of the lattice,

we determine the general parametric form of the exchange interaction matrices of a three-sublattice model and we provide the group theoretical reason behind the formation of the WF state. By solving the spin model we quantify the WF distortion in terms of the model parameters. Our results are clearly consistent with the original spin-model description of weak ferromagnetism in Mn$_3$Sn [1]; however, we exceed this approach by quantitative estimates on the WF distortion being in fairly good agreement with the experiments. We also obtain the magnetic ground states of the Mn$_3Z$ compounds from unconstrained self-consistent LDA calculations and investigate the effect of spin-orbit coupling (SOC) on the Mn and Z sites selectively. Finally, we give a hint to the effect of the induced moment at the Z site by performing constrained LDA calculations for the case of the Mn$_3$Ga alloy.

II. METHODS

A. Spin model

To study the magnetic properties of the Mn$_3Z$ alloys in the hexagonal phase, we use a classical Heisenberg model for the Mn spins represented with a set of unit vectors $\{\vec{e}\}$ and neglect the effect of the induced spin moment on the Z sites. The spin model in second order of the spin variables is given by

$$H(\{\vec{e}\}) = \sum_i \vec{e}_i \mathbf{K}_i \vec{e}_i - \frac{1}{2} \sum_{i \neq j} \vec{e}_i \mathbf{J}_{ij} \vec{e}_j , \quad (1)$$

where the i and j indices are confined to the Mn sites, $\mathbf{K}_i$ are the second order on-site anisotropy matrices, and $\mathbf{J}_{ij}$ are the tensorial exchange couplings. The exchange matrix can be decomposed as

$$\mathbf{J}_{ij} = J_{ij}\mathbf{I} + \tfrac{1}{2}\left(\mathbf{J}_{ij} - \mathbf{J}_{ij}^T\right) + \tfrac{1}{2}\left(\mathbf{J}_{ij} + \mathbf{J}_{ij}^T - 2J_{ij}\mathbf{I}\right) , \quad (2)$$

where $\mathbf{I}$ is the unit matrix and T denotes the transpose of a matrix. In the above decomposition, $J_{ij} = \frac{1}{3}\mathrm{Tr}\mathbf{J}_{ij}$ defines the isotropic Heisenberg coupling between two spins, the antisymmetric part of the exchange tensor can be related to the Dzyaloshinsky–Moriya interaction,

$$\vec{e}_i \tfrac{1}{2}\left(\mathbf{J}_{ij} - \mathbf{J}_{ij}^T\right)\vec{e}_j = \vec{D}_{ij}(\vec{e}_i \times \vec{e}_j), \quad (3)$$

and the traceless symmetric part of $\mathbf{J}_{ij}$ corresponds to the two-site anisotropy.

From previous experimental [1–3] and theoretical [15,19] works it turns out that the ground-state magnetic structure of the Mn$_3Z$ compounds can be well described in terms of an effective spin model related to three Mn sublattices. This means that the A–a, B–b, and C–c sublattice pairs (cf. Fig. 1) are strongly coupled ferromagnetically, ensuring that the corresponding Mn moments are parallel to each other. Consequently, we only have to consider three independent sublattices to explore the low-energy magnetic configurations. As will be shown in Sec. III A, our calculated exchange interactions clearly support this observation, which leads to the following simplified Hamiltonian:

$$H = -\frac{1}{2}\sum_{\alpha,\beta=1}^{3} \vec{e}_\alpha \mathbf{J}_{\alpha\beta} \vec{e}_\beta , \quad (4)$$
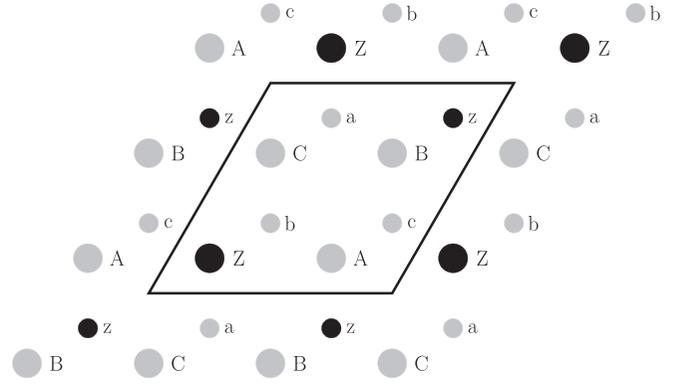
FIG. 1. The atomic positions in the hexagonal phase of the Mn$_3Z$ compounds: large and small circles, labeled by capital and small letters, denote sites in the atomic layers at $z = c/4$ and at $z = 3c/4$, respectively, while grey and black circles stand in order for Mn and Z atoms. The rhombus encloses a possible unit cell of the system.

where the $\mathbf{J}_{\alpha\beta}$ matrices are the effective sublattice interactions. The $\mathbf{J}_{\alpha\beta}$ matrices can be related to the exchange matrices in Eq. (1) as

$$\mathbf{J}_{\alpha\beta} = \sum_n \mathbf{J}_{0\alpha,n\beta} - 2\delta_{\alpha\beta}\mathbf{K}_\alpha , \quad (5)$$

where the index 0 stands for a fixed site in sublattice α, while n goes through the sites in sublattice β. Note that due to translation invariance, the on-site anisotropy matrices at all sites in a given sublattice are identical, which explains the notation $\mathbf{K}_\alpha$ in Eq. (5). By collecting the spin variables of the three sublattices into a nine-dimensional composite variable, $\vec{e} = (\vec{e}_1, \vec{e}_2, \vec{e}_3)$ and the sublattice interactions into a composite matrix,

$$\mathbf{J} = \begin{pmatrix} \mathbf{J}_{11} & \mathbf{J}_{12} & \mathbf{J}_{13} \\ \mathbf{J}_{21} & \mathbf{J}_{22} & \mathbf{J}_{23} \\ \mathbf{J}_{31} & \mathbf{J}_{32} & \mathbf{J}_{33} \end{pmatrix}, \quad (6)$$

Eq. (4) can be rewritten into the simple form

$$H = -\tfrac{1}{2}\vec{e}\,\mathbf{J}\,\vec{e} . \quad (7)$$

The structure of the matrices Eq. (5) can be obtained by using the D_{3h} point-group symmetry of the lattice. This is provided by the invariance of the energy of the spin system Eq. (4) against any point-group element $g \in D_{3h}$. Denoting the 9×9 matrix representation of g by $\mathbf{R}_g$, this implies the
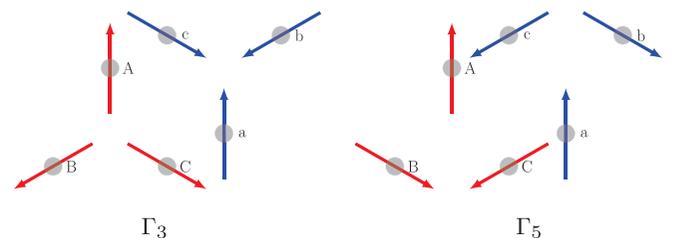
FIG. 2. Low-energy chiral magnetic structures of the Mn$_3Z$ compounds.

TABLE I. The experimental lattice constants for the Mn$_3Z$ compounds.

	Mn$_3$Sn [20]	Mn$_3$Ge [21]	Mn$_3$Ga [3]
a$_{2d}$[Å]	5.665	5.36	5.36
c/a	0.79982	0.80598	0.807

relationships

$$\mathbf{J} = \mathbf{R}_g^T \mathbf{J} \mathbf{R}_g . \tag{8}$$

Note that the permutation of the sublattices under the operation g is also included in the representation $\mathbf{R}_g$. Performing the corresponding analysis, we obtain two different types of sublattice interaction matrices: the three sublattice-diagonal matrices are connected via the C_3 rotation, while the six sublattice off-diagonal matrices are related to each other either by C_3 rotation or by transposition. One representative element for each set is given by

$$\mathbf{J}_{AA} = \begin{pmatrix} \frac{-K^x + 3K^y}{2} & 0 & 0 \\ 0 & \frac{3K^x - K^y}{2} & 0 \\ 0 & 0 & -K^x - K^y \end{pmatrix} \tag{9}$$

and

$$\mathbf{J}_{BC} = \begin{pmatrix} J + J^x & D & 0 \\ -D & J + J^y & 0 \\ 0 & 0 & J - J^x - J^y \end{pmatrix}, \tag{10}$$

respectively. The sublattice model therefore has six independent parameters: two sublattice-diagonal anisotropy constants, K^x and K^y, two sublattice-off-diagonal anisotropy constants, J^x and J^y, one Dzyaloshinsky–Moriya parameter, D, describing an effective DM vector parallel to the z axis, and an isotropic coupling between different sublattices, J. Note that in principle there is an isotropic coupling parameter for the sublattice-diagonal matrices, but it only adds a constant to the energy, thus it has no effect on the magnetic ordering in the system.

B. *Ab initio* calculations

We performed self-consistent electronic-structure calculations for the Mn$_3Z$ compounds in terms of the relativistic SKKR method [16,17]. The lattice constants of the different compounds were set to the experimental values shown in Table I.

We used the local spin-density approximation parametrized according to Vosko *et al.* [22] and we employed the atomic sphere approximation with an angular momentum cutoff of $\ell_{max} = 2$. We used 16 energy points on a semicircular path on the upper complex half-plane for the energy integrations and 144 points in the 2D Brillouin zone (2DBZ) for k integrations.

To obtain the parameters of the tensorial Heisenberg model Eq. (1), we employed the SCE developed originally by Drautz and Fähnle [23,24] combined with the RDLM method [25–27]. The RDLM method provides a first-principles description of a paramagnetic system according to the adiabatic decoupling of the electronic and spin degrees of freedom, while the SCE enables a systematic parametrization of the

TABLE II. Calculated isotropic couplings in the Mn$_3Z$ compounds. The interactions given in units of meV are indexed according to increasing distances of the pairs, while interactions with and without prime stand for inequivalent pairs with the same distance (see Fig. 3). For better understanding, in the second row, the in-plane and out-of-plane couplings are denoted by ip and oop, respectively.

	J_1 oop	J_2 ip	J_2' ip	J_3 oop	J_3' oop	J_4 oop	J_5 oop
Mn$_3$Sn	−15.3	−3.2	4.5	13.8	11.3	−2.87	−4.08
Mn$_3$Ge	−22.6	−7.4	10.1	5.9	7.1	−2.54	−4.39
Mn$_3$Ga	−23.7	−15.9	0.9	10.7	5.5	−3.82	−4.42

adiabatic energy surface. For the details of the SCE-RDLM method, see Ref. [18]. In the SCE calculations, we used 16 energy points on a semicircular path on the upper complex half-plane with approximately 20 000 k points in the 2DBZ near the Fermi energy.

III. RESULTS

A. Spin model parameters

We applied the SCE-RDLM method to obtain the *ab initio* spin model parameters in the paramagnetic phase of each compound. First, we discuss the isotropic couplings. In Table II, we show the first five nearest-neighbor interactions as visualized in Fig. 3. For all three compounds, we find a similar structure of the isotropic interactions. The nearest-neighbor interactions J_1 couple sites that belong to different sublattices and different atomic layers. They are AFM and the largest in magnitude among the isotropic couplings. By contrast, the third nearest-neighbor out-of-plane interactions, J_3 and J_3', that connect sites in the same sublattice are strongly ferromagnetic. These interactions thus force aligning the moments in the same sublattice irrespective of the atomic-layer positions. On top of this, the AFM first nearest-neighbor couplings cause frustration on the kagome lattice and stabilize the triangular states as shown in Fig. 2. The (in-plane) second-nearest-neighbor AFM interactions, J_2, also contribute to the
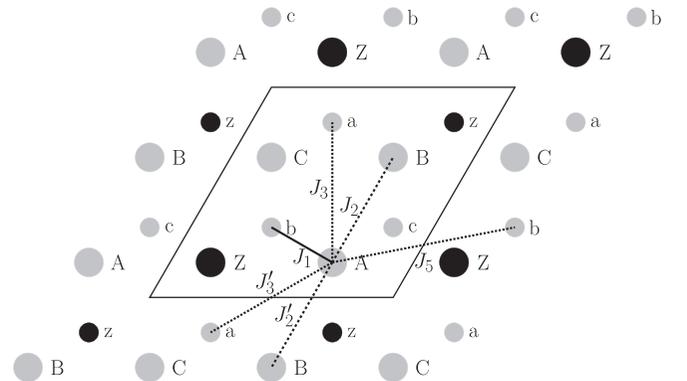
FIG. 3. Schematic view of the first five nearest-neighbor interactions. Different interactions for the same distance are denoted with and without primes. The J_4 interaction connects two sites in the same sublattice from neighboring unit cells shifted along the z axis, thus, we could not illustrate it in the figure.
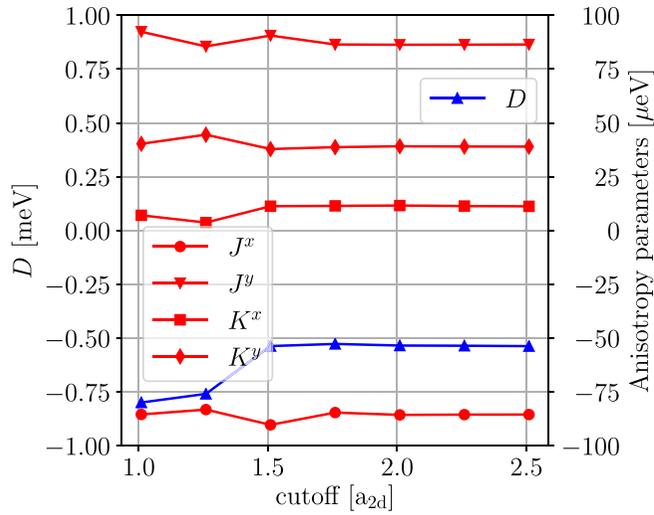
FIG. 4. The cutoff dependence of the relativistic interactions in the sublattice matrices Eqs. (9) and (10) for Mn_3Sn. Note that the DM parameter D is about one order of magnitude larger than the anisotropy parameters. The isotropic coupling J (not presented here) shows a similar cutoff dependence.

stabilization of the triangular spin structures, though the other type of these interactions, J_2', is ferromagnetic, destabilizing the triangular state to some extent. By using the *ab initio* tensorial spin model, we solved the Landau–Lifshitz–Gilbert equations at zero temperature (with damping term only) and for all three compounds we indeed obtained a ground state close to the Γ_5 state. As we will demonstrate later, it is the DM interaction which selects between the Γ_3 and Γ_5 spin states.

From the $\mathbf{J}_{ij}$ and $\mathbf{K}_i$ matrices we can calculate the $\mathbf{J}_{\alpha\beta}$ matrices as defined in Eq. (5). We checked that the obtained matrices satisfy to high accuracy the analytic forms Eqs. (9) and (10) we deduced from symmetry principles, so the six parameters of the sublattice model can be read off. The values of these parameters depend on the cutoff distance of pairs in the sum in Eq. (5). The dependence of the DM and the anisotropy parameters for Mn_3Sn is shown in Fig. 4. Clearly, all parameters converge well beyond a distance of about $2\,a_{2d}$. The other two compounds show similar behavior. Based on these results, in all cases we used a cutoff of $2.51\,a_{2d}$ for the calculation of the sublattice model parameters.

The calculated parameters of the sublattice model, see Eqs. (9) and (10), are summarized in Table III. In each case, a large AFM isotropic coupling was obtained, which again explains the formation of the low-energy frustrated triangular configurations. The DM parameter being two orders of

TABLE III. Calculated sublattice model parameters, see Eqs. (9) and (10), for the Mn_3Z compounds based on the SCE-RDLM method.

	J[meV]	D[meV]	K^x[μeV]	K^y[μeV]	J^x[μeV]	J^y[μeV]
Mn_3Sn	−46.7	−0.547	11	39	−85	86
Mn_3Ge	−51.6	−0.246	−64	123	−108	92
Mn_3Ga	−77.0	−0.447	−8	129	−65	135
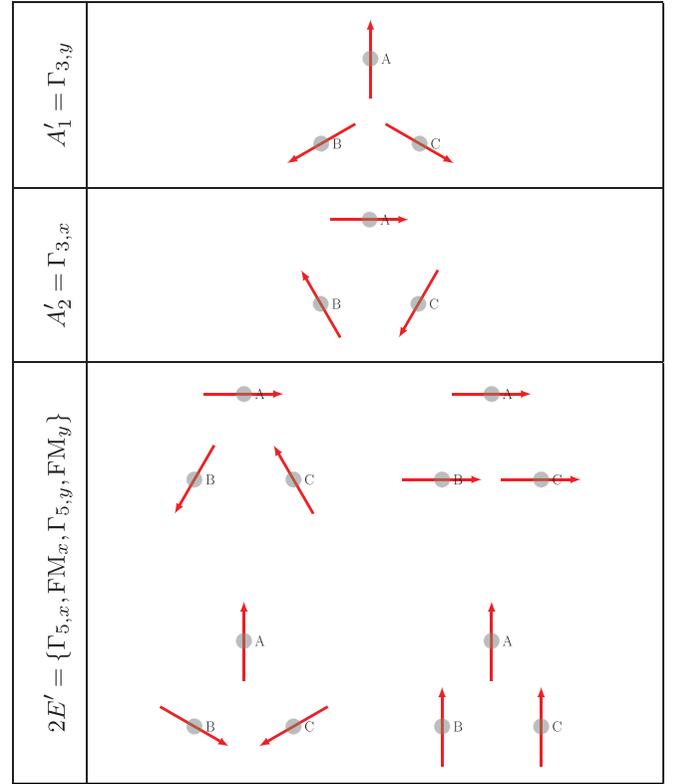
FIG. 5. The irreducible representations corresponding to the low-energy spin configurations within the nine-dimensional subspace of the three Mn sublattices.

magnitude less than J has negative sign, thus, it prefers the Γ_5 state against the Γ_3 state for all of the compounds. The anisotropy constants are typically one order of magnitude less than the DM parameters. Remarkably, the anisotropy parameters indexed by x are positive and those indexed by y are negative. The only exception is observed for K^x in case of Mn_3Sn, which is negative in sign.

B. Group-theoretical argument

The representation $\mathbf{R}_g$ of the D_{3h} point group on the nine-dimensional space defined within the three-sublattice model, see Eqs. (7) and (8), can be decomposed according to irreducible representations as

$$\mathbf{R}_g = A_1' \oplus A_2' \oplus 2E' \oplus A_2'' \oplus E'' , \qquad (11)$$

where A_1', A_2', and A_2'' are one-dimensional, while E' and E'' are two-dimensional irreducible representations. After projecting to irreducible subspaces, we found that the low-energy chiral states and the ferromagnetic states correspond to the A_1', A_2', and the $2E'$ irreducible representations as shown in Fig. 5. Here we distinguish the states $\Gamma_{3,x}$, $\Gamma_{3,y}$ and $\Gamma_{5,x}$, $\Gamma_{5,y}$ based on the orientation of the spin on the A sublattice.

From Fig. 5, we can conclude that the states $\Gamma_{3,x}$ and $\Gamma_{3,y}$ correspond to different one-dimensional irreducible representations, therefore, they are not degenerate by symmetry. So the energy of the Γ_3 states changes under in-plane global rotations. In contrast, the $\Gamma_{5,x}$ and $\Gamma_{5,y}$ states and also the FM_x and FM_y states form the basis of the same two-dimensional

irreducible representation (E'), thus, they are pairwise degenerate. This means that the Γ_5 and FM states are energetically insensitive to in-plane global rotations. Furthermore, sharing the same symmetry, the $\Gamma_{5,x}$ and the FM$_x$ states are coupled and the same applies to the $\Gamma_{5,y}$ and the FM$_y$ states. To obtain the ground state of the model, we have to diagonalize the Hamiltonian Eq. (7) in the corresponding subspaces, which leads to the diagonalization of the following matrix:

$$\begin{pmatrix} \vec{e}_{\Gamma_{5,\xi}} \, \mathbf{J} \, \vec{e}_{\Gamma_{5,\xi}} & \vec{e}_{\Gamma_{5,\xi}} \, \mathbf{J} \, \vec{e}_{\text{FM}_\xi} \\ \vec{e}_{\text{FM}_\xi} \, \mathbf{J} \, \vec{e}_{\Gamma_{5,\xi}} & \vec{e}_{\text{FM}_\xi} \, \mathbf{J} \, \vec{e}_{\text{FM}_\xi} \end{pmatrix}, \quad (12)$$

where $\xi \in \{x, y\}$. The four resulting eigenstates can be cast into two degenerate WF states that are slight distortions of the Γ_5 states and two degenerate states that are modulations of the FM states. The low-energy WF eigenstates can be written as

$$\vec{e}_{\text{WF}_x} = \mu \, \vec{e}_{\Gamma_{5,x}} + \nu \, \vec{e}_{\text{FM}_x}, \quad (13)$$

$$\vec{e}_{\text{WF}_y} = \mu \, \vec{e}_{\Gamma_{5,y}} - \nu \, \vec{e}_{\text{FM}_y}, \quad (14)$$

where $\mu^2 + \nu^2 = 1$ and the explicit analytical expression for the ν parameter in terms of the sublattice model parameters indicates that

$$\nu \propto (J^x - J^y) + 2(K^x - K^y). \quad (15)$$

This result also suggests that the two different WF states possess a net magnetization of $\pm \nu$ coming from their FM component, indicating that the direction of this WF moment with respect to the A moment is different in the x and y cases. Moreover, the WF moment appears only if the x and y on-site and/or two-site anisotropy parameters differ from each other, but it does not occur if only the DM interaction (DMI) is present in the system on top of the AFM isotropic interactions. Thus, in terms of group theoretical analysis, we regained the result of Tomiyoshi and Yamaguchi [1], stating that the formation of the weak ferromagnetism in the Mn$_3$Sn compound happens due to magnetic anisotropy rather than DMI. We note that the WF states Eqs. (13) and (14) are stationary states of the Hamiltonian Eq. (7) with the lowest energy, but they do not refer to a set of spin vectors of unit length assumed in the classical Heisenberg model. In the next section, we therefore revisit our investigation of the WF states within the space of classical spin states.

C. Classical spin-model study

As discussed in the previous section in terms of group-theoretical arguments, the energy of the Γ_3 state shows anisotropic behavior under global rotations around the z axis, while the energy of the Γ_5 state is invariant to such rotations. This can be easily shown by calculating the rotational energies directly from Eq. (4) and using the parametric forms of the sublattice exchange matrices, Eqs. (9) and (10). For the Γ_3 state, this gives

$$E_{\Gamma_3}(\phi) = \frac{3}{2}\left(J - \sqrt{3}D + \frac{3J^x - J^y}{2} - \frac{3K^x - K^y}{2}\right)$$
$$+ 3(K^x - K^y - J^x + J^y)\sin^2\phi, \quad (16)$$

where ϕ is the rotation angle around the z axis with respect to the y direction of the magnetic moment at the A atom (see
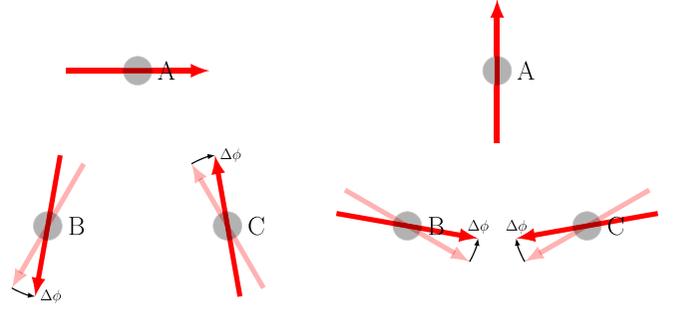
FIG. 6. Weak ferromagnetic distortions of the Γ_5 states: the WF$_x$ state on the left and the WF$_y$ state on the right. The shaded arrows show the spin directions in the original Γ_5 state. The distortion is parametrized by the tilting angle $\Delta\phi$.

the left panel of Fig. 2). From the data of Table III, it can be inferred that the in-plane anisotropy constant defined as the coefficient of the $\sin^2\phi$ term is positive, so the $\phi = 0$ state ($\Gamma_{3,y}$) is the lowest in energy. For the energy of the Γ_5 states, we get a constant indeed:

$$E_{\Gamma_5} = \frac{3}{2}\left(J + \sqrt{3}D + \frac{J^x + J^y}{2} - \frac{K^x + K^y}{2}\right). \quad (17)$$

The energy difference between the Γ_5 and the $\Gamma_{3,y}$ states is then given by

$$E_{\Gamma_5} - E_{\Gamma_{3,y}} = 3\sqrt{3}D + \frac{3}{2}(K^x - K^y - J^x + J^y). \quad (18)$$

Since for all considered Mn$_3$Z compounds the DMI is negative and is much larger in magnitude than the in-plane anisotropy term entering Eq. (18), in each case the Γ_5 state has lower energy than the Γ_3 state. This should be contrasted with the $L1_2$-type Mn$_3$Ir alloy, where the Γ_3 state is stabilized due to the magnetic anisotropy of about 10 meV [28].

Within the classical spin model, the WF distortions can be parametrized by a tilting angle $\Delta\phi$ for two of the sublattices as illustrated in Fig. 6. The WF moment is then related to $\Delta\phi$ as

$$m_{\text{WF}}(\Delta\phi) = 1 - 2\sin\left(\frac{\pi}{6} - \Delta\phi\right). \quad (19)$$

We calculated the energy of the WF states as a function of the tilting angle $\Delta\phi$ based on the sublattice spin model. The corresponding energy curves are shown in Fig. 7 for both the WF$_x$ and WF$_y$ distortions and for all three compounds. As expected, for each alloy, a clear parabolic minimum is obtained with positive $\Delta\phi$ for WF$_x$ distortions and with negative $\Delta\phi$ for WF$_y$ distortions (cf. Fig. 6). The WF moments and the distortion angles obtained from the minima of the energy curves in Fig. 7 are summarized in Table IV. Interestingly, the magnitudes of the WF$_x$ tilting angle are systematically smaller than those for WF$_y$, although the relative difference is about or less than 1%. Correspondingly, the size of the WF moments also somewhat differ for the two kinds of WF distortions, which contradicts the prediction of the group-theoretical analysis. It should be recalled again that the ground state obtained from group theory is outside the space of classical spin states.

We also note that the WF$_x$ and WF$_y$ states are no longer degenerate within the classical spin model. Our numerical
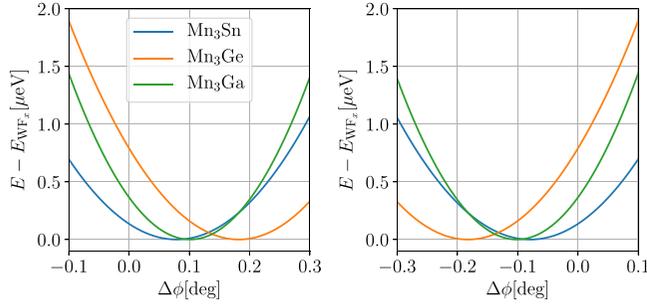
FIG. 7. Calculated energy curves for the Mn$_3Z$ compounds as a function of the $\Delta\phi$ weak ferromagnetic distortion angle. Left: WF$_x$ state, right: WF$_y$ state. For all three alloys, both energy curves are shifted by the minimum of the corresponding WF$_x$ curve, E_{WF_x}.

calculations showed that the WF$_y$ state is deeper in energy than the WF$_x$ state. The reason for this is that the local easy axes of the Mn atoms correspond to the spin directions in the $\Gamma_{3,y}$ state, see Fig. 6, as the magnetic anisotropy constant per Mn atom $K^x - K^y - J^x + J^y$ is positive for all the three compounds. According to our numerical calculations, see also Fig. 7, the energy difference between the two WF states is, however, in the order of 10^{-9} eV/f.u.

To gain deeper insight into the results obtained above and on the relationship of the WF distortion angle and the parameters of the spin model, we repeated the search for the minimum of the WF distortion energy analytically. The energy of the WF$_x$ distortion can be expressed as

$$
\begin{aligned}
E_{WF_x}(\Delta\phi) = {} & J(\cos(2\Delta\phi - \pi/3) + 2\cos(\Delta\phi + \pi/3)) \\
& - D(\sin(2\Delta\phi - \pi/3) - 2\sin(\Delta\phi + \pi/3)) \\
& + \frac{J^x}{2}(\cos(2\Delta\phi - \pi/3) + 2\cos(\Delta\phi) - 1) \\
& + \frac{J^y}{2}(\cos(2\Delta\phi - \pi/3) - 2\sqrt{3}\sin(\Delta\phi) + 1) \\
& - (K^x - K^y)\cos(2\Delta\phi + \pi/3) - \frac{K^x}{4} - \frac{5K^y}{4},
\end{aligned}
\tag{20}
$$

and similar for $E_{WF_y}(\Delta\phi)$ by interchanging indices x and y. After expanding the above expression up to second order in $\Delta\phi$, it is easy to find its minimum, yielding

$$
\Delta\phi_x = -\frac{\sqrt{3}}{2}\frac{J^x - J^y + 2(K^x - K^y)}{-3J - 3\sqrt{3}D - 2J^x - J^y + 2K^x - 2K^y}
\tag{21}
$$

and again similar for $\Delta\phi_y$ by interchanging the indices x and y.

TABLE IV. Calculated weak ferromagetic distortions and net magnetic moments for the Mn$_3Z$ compounds from the sublattice spin model with parameters obtained using the SCE-RDLM method.

	$\Delta\phi_x$[deg]	$m_{WF_x}[10^{-3}]$	$\Delta\phi_y$[deg]	$m_{WF_y}[10^{-3}]$
Mn$_3$Sn	0.0785	2.37	−0.0795	−2.40
Mn$_3$Ge	0.1821	5.51	−0.1825	−5.51
Mn$_3$Ga	0.1009	3.05	−0.1018	−3.06

This result has some important implications. First, the numerator on the right-hand side of Eq. (21) changes signs between the WF$_x$ and WF$_y$ distortions, while the denominator is always positive due to the large negative J and D parameters, which uniquely explains the sign change between the distortion angles $\Delta\phi_x$ and $\Delta\phi_y$. In addition, there is a small change in the denominator for the x and y cases, so we also found an analytic explanation for the deviation in the size of the corresponding tilting angles in Table IV. Second, the numerator is identical to the multiplicative factor we obtained from group theory for the WF moment, see Eq. (15). If we expand Eq. (19) around $\Delta\phi = 0$, we can see that for small distortions the WF moment m_{WF} is proportional to $\Delta\phi$, thus also with $J^x - J^y + 2(K^x - K^y)$ as proposed by group theory. The weak ferromagnetism in the Mn$_3Z$ alloys is, therefore, qualitatively explained in the same way from group theory and from the classical spin model as being the consequence of nonzero on-site and/or two-site anisotropies, $K^x - K^y$ and $J^x - J^y$, respectively.

D. Self-consistent calculations

We also performed self-consistent calculations to determine the ground states of the Mn$_3Z$ alloys by using the relativistic SKKR approach. We use the setup for the SKKR calculations discussed in Sec. II B and we let the magnetic moments relax from the $\Gamma_{5,x}$ and $\Gamma_{5,y}$ states to the corresponding WF states. This way, we include the effect of the induced moment on the Z sites and also orbital-polarization effects into the calculations similar to the work of Sandratskii and Kübler [15], who investigated the weak ferromagnetism of Mn$_3$Sn from *ab initio* calculations.

In Table V, we summarize the main results of the SKKR calculations for the WF states of the Mn$_3Z$ compounds. First, we observe that the distortion of the spin vectors for Mn$_3$Sn is opposite for both the WF$_x$ and WF$_y$ states as proposed by the spin model, see Table IV. Regarding the expressions we derived for the distortion angles, Eq. (21), this would mean that the self-consistent calculations predicted a magnetic anisotropy of opposite sign as compared to the spin model obtained from the SCE method. From Fig. 8 presenting the spin and orbital contributions to the WF moments we, however, see that in case of Mn$_3$Sn, the WF moment is dominated by the orbital moment to which the spin model does not apply. In this case, the tilting of spin moments seems to follow that of the orbital moments. Reassuringly, Sandratskii and Kübler [15] also obtained distortions of the same rotational sense for the WF$_x$ and WF$_y$ states, resulting in a net moment antiparallel and parallel with the moment of the A atom, respectively. In contrast to our work, the spin-moment contribution reported in Ref. [15] is almost twice as large as the orbital contribution, though the total WF moment, 0.004 μ_B, is very close to our value (0.003 μ_B). Remarkably, the distortion angle of the orbital moments is about two orders of magnitude larger than that of the spin moments, which, at least to a somewhat smaller extent, was also found in Ref. [15]. It is worth it to note that the SKKR codes rely on the solution of the Kohn–Sham–Dirac equation, while in Ref. [15] the SOC is treated as an additive term to a scalar-relativistic Hamiltonian [32].

TABLE V. The properties of the self-consistent weak ferromagnetic ground states of the Mn$_3$Z compounds calculated from the SKKR method. The experimental results are taken from Refs. [3,21,31] for Mn$_3$Sn, Mn$_3$Ge, and Mn$_3$Ga, respectively. The sign of the weak ferromagnetic moments refers to their orientation relative to the orientation of the moments in the A sublattice, see Fig. 6.

	Mn$_3$Sn	Mn$_3$Ge	Mn$_3$Ga
$\Delta\phi_x$	spin: $-0.006°$ orbital: $-0.74°$	spin: $0.052°$ orbital: $6.9°$	spin: $0.22°$ orbital: $10.5°$
$\Delta\phi_y$	spin: $0.010°$ orbital: $0.78°$	spin: $-0.065°$ orbital: $-5.9°$	spin: $-0.39°$ orbital: $-8.9°$
$m_s^{Mn}[\mu_B]$	3.15 (3.17 ± 0.07 exp.)	2.61 (2.4 ± 0.2 exp.)	2.60 (2.4 ± 0.2 exp.)
$m_{WF}[\mu_B]$	x: -0.003, y: 0.003 (0.009 exp.)	x: 0.016, y: -0.017 (0.06 exp.)	x: 0.030, y: -0.041 (0.045 exp.)
$E_{WF_x} - E_{WF_y}$[eV/f.u.]	$8.9 \cdot 10^{-8}$	$-3 \cdot 10^{-9}$	$-4.7 \cdot 10^{-6}$

For Mn$_3$Ge and Mn$_3$Ga, the self-consistent calculations yield WF distortions of the same direction as found in the spin-model studies although, for Mn$_3$Ge, the orbital contribution is still nearly three times larger than the orbital contribution, see Fig. 8. Only in the case of Mn$_3$Ga, the spin-moment contributions become dominant and, curiously, this contribution shows a large difference between the WF$_x$ and WF$_y$ states which cannot be understood based on the sublattice spin model. By contrast, the orbital contributions do not show this asymmetry for any of the systems under investigation, even though the quite enhanced distortion angles of the orbital moments for Mn$_3$Ge and Mn$_3$Ga display a remarkable anisotropy. As also indicated in Table V, our *ab initio* calculations can not resolve with a reliable accuracy which of the two kinds of WF states is energetically preferred. In case of Mn$_3$Ga, the WF$_x$ seems to be lower in energy, but from the very small energy difference of $4.7 \cdot 10^{-6}$ eV/f.u., we rather conclude that the two WF states are degenerate within the precision of the method we use.

A comparison with the experimental results is also shown in Table V. The calculated spin moments of the Mn atoms are within the error range of the experiments. We note that the Mn moments slightly differ on the A and B (or C) sublattices as also reported in Ref. [15]. The calculated WF moments are also in the range of the experimental values. The smallest
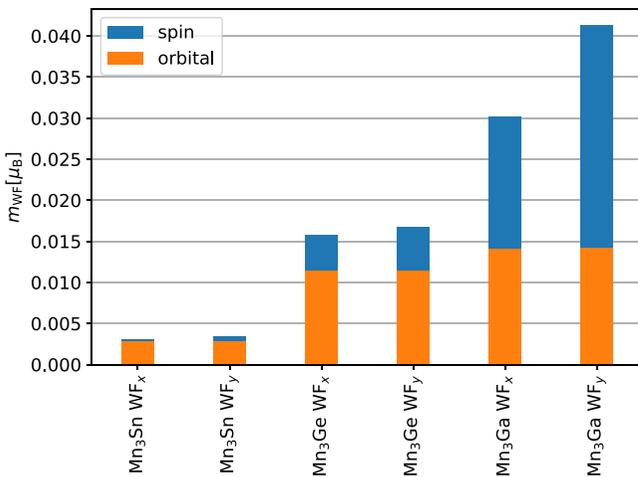
value is obtained for Mn$_3$Sn as in the experiment, while for Mn$_3$Ga we find a very good quantitative agreement with the measured value. The largest deviation from the experiment is found in the case of Mn$_3$Ge. A fair comparison between theory and experiment is, however, hardly possible for this alloy, since only off-stoichiometric samples could be prepared [21], where Mn atoms can occupy Z positions leading to an enhanced net magnetic moment. Zhang *et al.* [10] also performed density-functional calculations using VASP [29] for the hexagonal Mn$_3$Z alloys. As compared to their results, our calculated Mn spin moments are systematically larger by about 0.1 μ_B, which might be attributed to the fact that in Ref. [10], slightly smaller, optimized lattice constants and the generalized gradient approximation for the exchange-correlation functional [30] were used as opposed to the experimental lattice constants and the local density functional we employed, respectively. Reassuringly, however, they reported the WF moments, 0.01 μ_B for Mn$_3$Sn and Mn$_3$Ge and 0.03 μ_B for Mn$_3$Ga, that are consistent with our values.

As we noted already, the orbital moments have a significant weight in the WF moment. Interestingly, the orbital moments of the Mn atoms show the behavior we found from group theory, namely that the WF state can be decomposed as the linear combination of a Γ_5 and an FM state with the same mixing coefficients for the x and y state as given in Eqs. (13) and (14). In correspondence with these relationships, the net orbital moments for the WF$_x$ and WF$_y$ states are $m_\ell^{Mn} = 3\nu$ and $m_\ell^{Mn} = -3\nu$, respectively, while subtracting $\vec{m}_\ell^{Mn}/3$ from the orbital moments of each sublattice, a perfect Γ_5 state is obtained with local orbital moments of μ. The corresponding parameters for the three alloys are collected in Table VI. The opposite sign of ν for Mn$_3$Sn as compared to Mn$_3$Ge and Mn$_3$Ga reflects the opposite sign of the tilting angle as discussed above. Moreover, the increased magnitudes of ν/μ for Mn$_3$Ge and Mn$_3$Ga correspond to the enhanced tilting angles for these alloys with respect to Mn$_3$Sn, see Table V.

FIG. 8. Self-consistently calculated spin and orbital contributions to the weak ferromagnetic moments for the Mn$_3$Z alloys. The moments are shown for both the WF$_x$ and WF$_y$ states.

TABLE VI. The μ and ν parameters for the self-consistently calculated orbital moments, see Eqs. (13) and (14), using the convention where the Γ_5 and FM states are constructed from dimensionless unit vectors and the parameters are measured in units of $10^{-3}\mu_B$.

	Mn$_3$Sn	Mn$_3$Ge	Mn$_3$Ga
μ	40	33	26
ν	-0.6	4.3	x: 5.07 y: -5.10

TABLE VII. Self-consistently calculated net magnetic moments of the weak ferromagnetic states in the Mn_3Z alloys decomposed into spin and orbital contributions, as well as into contributions related to the Mn and Z atoms. All values are given in units of $10^{-3}\mu_B$. Both the WF_x and WF_y states are considered (see the second column). The cases when the SOC is included on all sites, only on the Mn sites and only on the Z sites, are indicated in the third column by all, Mn, and Z, respectively (Z = Sn, Ge, Ga).

		SOC	m_s^{Mn}	m_s^Z	m_s	m_ℓ^{Mn}	m_ℓ^Z	m_ℓ
Mn_3Sn	WF_x	all	−0.13	−0.01	−0.14	−1.80	−1.04	−2.84
		Mn	1.58	−0.03	1.56	9.73	−0.99	8.74
		Sn	0.24	0.01	0.25	−11.47	−0.07	−11.53
	WF_y	all	0.49	0.01	0.49	1.80	1.04	2.85
		Mn	−1.66	0.03	−1.63	−9.73	0.99	−8.74
		Sn	−0.24	−0.01	−0.25	11.47	0.07	11.53
Mn_3Ge	WF_x	all	4.43	−0.08	4.36	12.79	−1.32	11.47
		Mn	6.13	−0.09	6.04	18.65	−1.23	17.42
		Ge	−0.14	0.00	−0.13	−5.89	−0.09	−5.98
	WF_y	all	−5.39	0.10	−5.30	−12.81	1.32	−11.49
		Mn	−7.98	0.11	−7.86	−18.69	1.23	−17.45
		Ge	0.11	−0.00	0.11	5.89	0.09	5.98
Mn_3Ga	WF_x	all	16.33	−0.33	16.00	15.22	−1.11	14.11
		Mn	24.38	−0.50	23.88	20.41	−1.03	19.38
		Ga	33.83	−0.70	33.13	−5.21	−0.08	−5.29
	WF_y	all	−27.57	0.55	−27.02	−15.33	1.11	−14.22
		Mn	−38.97	0.77	−38.20	−20.57	1.03	−19.54
		Ga	−21.69	0.43	−21.26	5.21	0.08	5.29

Note that for Mn_3Ga, we found a slight deviation from the decomposition based on Eqs. (13) and (14). We believe that this impressive agreement between the distortion of the orbital moments and the group-theoretical prediction is due to the strongly nonrigid character of the orbital moments. The lack of a constraint of a constant magnitude allows the orbital moments to assume the superimposed WF configuration preferred by group theory.

Within the KKR formalism, it is possible to scale down the SOC selectively on different sites using a scalar relativistic framework for the treatment of the single-site scattering [32,33]. To gain more insight into the effect of the spin-orbit coupling, we performed self-consistent calculations for each compound where we switched off the SOC either on the Z or on the Mn sites. The results for the calculated spin and orbital parts of the net moments and their resolution into the Mn- and Z-atom contributions are summarized in Table VII together with the case where the SOC is included at all sites.

First, Table VII indicates that net orbital moments induced by the SOC at the Mn and at the Z atoms add up almost perfectly when the SOC is switched on at each of the sites. Moreover, this is valid for the site-resolved contributions of the net orbital moments. Apparently, such an additivity of the SOC induced net spin moments can not be established.

In the case of Mn_3Sn, the SOC at the Mn sites induces a sizable net spin moment mainly with contributions from the Mn atoms, but superimposed with the SOC of Sn, this spin moment considerably reduces in size and it also changes signs. By contrast, the SOC of Sn raises an orbital moment of about 0.01 μ_B in size, originating from the Mn atoms, which is, however, largely compensated by the orbital moment of opposite sign induced by the SOC of the Mn atoms. Although some orbital moment is induced also at the Sn sites being

parallel to the orbital moment of the Mn atoms induced by the SOC of Sn, the total orbital moment remains parallel to that induced by the SOC of Mn. This peculiar cancellation of the orbital moments was also noticed and discussed by Sandratskii and Kübler [15].

In the case of the Mn_3Ge and the Mn_3Ga alloys, it remains valid that both the net spin and orbital moments mostly have contributions from the Mn atoms, while the Ge and Ga atoms add a negligible amount especially to the spin moment. The SOC of Mn plays a dominant role in the formation of the net moments in Mn_3Ge and this effect is only compensated in about 30% by the SOC of Ge. This explains the opposite direction of the WF distortion and, correspondingly, the opposite direction of the net moment as compared to Mn_3Sn, where the effect of the SOC of Sn dominates. The SOC of both the Mn and Ga atoms have a large effect in inducing a net spin moment in Mn_3Ga, but, interestingly, when switching on the SOC simultaneously on both sites, the total spin moment is much less than the sum of the spin moments for selectively switched SOC. Moreover, the size of the spin moments induced by the SOC of Mn and Ga follow an opposite order for the WF_x and WF_y states, which might be connected with the large asymmetry of the spin moments for these WF states in Mn_3Ga.

The origin of the large asymmetry of the WF spin moments for the WF_x and WF_y states obtained from the self-consistent density-functional calculations is an unresolved issue. The largest anisotropy is found for Mn_3Ga, where also the largest induced spin moment at the Z atom is observed, likewise with a remarkably large asymmetry. To see whether there is a connection between these two effects, we performed self-consistent calculations by applying a longitudinal constraining field at the Ga site by which the spin moment of
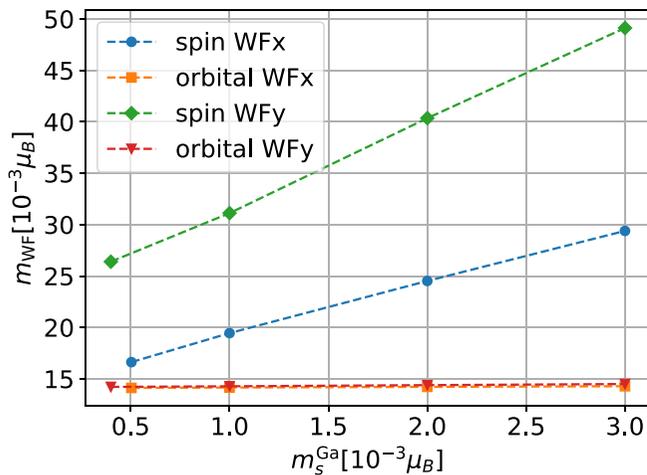
FIG. 9. Magnitudes of the spin and the orbital contributions to the weak ferromagnetic moment in Mn$_3$Ga as a function of the induced spin moment at the Ga site in Mn$_3$Ga obtained from self-consistent constraining field calculations.

Ga could be set arbitrarily. In Fig. 9, we plotted the net spin and orbital moments as a function of the induced spin moment on the Ga site. Or results indicate that the induced moment of Ga affects the net orbital moment only very moderately. By contrast, the net spin moments increase nearly linearly with the induced moment of Ga. The corresponding lines for the WF$_x$ and WF$_y$ states have a different slope, which implies that the asymmetry is also increasing with increasing induced moment of Ga. Extrapolating the lines to $m_s^{Ga} = 0$ there still remains a difference, $m_{WF_y} - m_{WF_x} \simeq 10^{-2}\mu_B$, therefore, we can at best conclude that the induced moment of Ga is one of the sources of the asymmetry of the WF moment in Mn$_3$Ga. The linear increase of the net spin moment with m_s^{Ga} can qualitatively be understood in terms of an isotropic exchange coupling between the Mn and Ga spin moments, while the asymmetry of the net spin moments can be attributed to the anisotropy, i.e., to the tensorial nature of this coupling.

IV. CONCLUSIONS

We studied the weak ferromagnetism in the Mn$_3$Z (Z = Sn, Ge, Ga) alloys using a combination of *ab initio* and spin model calculations. Using the point-group symmetry of the

systems, we set up a model for the three Mn sublattices including the relativistic terms of the Heisenberg Hamiltonian. The parameters of this model were obtained from *ab initio* calculations relying on a SCE. Based on a group-theoretical analysis we showed that there are two degenerate ground states, WF$_x$ and WF$_y$, being the mixture of the Γ_5 and FM states. The analytical forms of the mixing coefficients imply that the WF states will only form if the anisotropy parameters distinguish between the x and y spin directions. We recovered this result from analytical expressions for the energy within the classical spin model. Our presented results are fully consistent with the original spin model description of weak ferromagnetism in Mn$_3$Sn by Tomiyoshi and Yamaguchi [1].

We also performed self-consistent relativistic local density-functional calculations to investigate the WF states in a more involved way. In agreement with the seminal work for Mn$_3$Sn by Sandratskii and Kübler [15], our results highlighted the significance of the orbital moments in the weak ferromagnetism of the Mn$_3$Z alloys. A key observation from our calculations is that, as opposed to the spin moments, the orbital moments almost strictly follow the decomposition according to irreducible representations as predicted by group theory. As far as the spin moments of the Mn atoms and the WF moments are concerned, we found a good agreement with the experiments for all the three alloys. The only exception is the net magnetic moment of Mn$_3$Ge, where presumably due to the off-stoichiometry of the samples the measured moment is significantly higher than the theoretical one [10]. By switching on the SOC at different sites selectively, we discussed the role of the SOC on the formation of WF moments and recovered the peculiar cancellation of orbital moments for Mn$_3$Sn reported in Ref. [15], while we also found an argument for the opposite WF distortion as compared to Mn$_3$Ge and Mn$_3$Ga. By using constrained local density-functional calculations, we established that the induced spin moment of Ga plays an important role in the formation of the WF moment in Mn$_3$Ga and also is one of the reasons for the observed large asymmetry of the net moment concerning the WF$_x$ and WF$_y$ states.

[1] S. Tomiyoshi and Y. Yamaguchi, J. Phys. Soc. Jpn. **51**, 2478 (1982).

[2] S. Tomiyoshi and Y. Yamaguchi, J. Magn. Magn. Mater. **31-34**, 629 (1983).

[3] E. Krén and G. Kádár, Solid State Commun. **8**, 1653 (1970).

[4] J. Kübler and C. Felser, Europhys. Lett. **108**, 67001 (2014).

[5] S. Nakatsuji, N. Kiyohara, and T. Higo, Nature **527**, 212 (2015).

[6] A. K. Nayak, J. E. Fisher, Y. Sun, B. Yan, J. Karel, A. C. Komarek, C. Shekhar, N. Kumar, W. Schnelle, J. Kübler, C. Felser, and S. S. P. Parkin, Sci. Adv. **2**, e1501870 (2016).

[7] J. Kübler and C. Felser, Europhys. Lett. **120**, 47002 (2017).

[8] H. Yang Y. Sun, Y. Zhang, S. S. P. Parkin, and B. Yan, New J. Phys. **19**, 015008 (2017).

[9] A. Hirohata, T. Huminiuc, J. Sinclair, H. Wu, M. Samiepour, G. Vallejo-Fernandez, K. O'Grady, J. Balluf, M. Meinert, G. Reiss, E. Simon, S. Khmelevskyi, L. Szunyogh, R. Yanes Díaz, U. Nowak, T. Tsuchiya, T. Sugiyama, T. Kubota, K. Takanashi, N. Inami, and K. Ono, J. Phys. D: Appl. Phys. **50**, 443001 (2017).

[10] D. Zhang, B. Yan, S.-C. Wu, J. Kübler, G. Kreiner, S. S. P. Parkin, and C. Felser, J. Phys.: Cond. Matt. **25**, 206006 (2013).

[11] S. Khmelevskyi, A. V. Ruban, and P. Mohn, Phys. Rev. B **93**, 184404 (2016).

[12] I. Dzyaloshinskii, J. Phys. Chem. Solids **4**, 241 (1958).

[13] T. Moriya, Phys. Rev. **120**, 91 (1960).

[14] E. Mendive-Tapia and J. B. Staunton, Phys. Rev. B **99**, 144424 (2019).

[15] L. M. Sandratskii and J. Kübler, Phys. Rev. Lett. **76**, 4963 (1996).

[16] L. Szunyogh, B. Újfalussy, P. Weinberger, and J. Kollár, Phys. Rev. B **49**, 2721 (1994).

[17] R. Zeller, P. H. Dederichs, B. Újfalussy, L. Szunyogh, and P. Weinberger, Phys. Rev. B **52**, 8807 (1995).

[18] L. Szunyogh, L. Udvardi, J. Jackson, U. Nowak, and R. Chantrell, Phys. Rev. B **83**, 024401 (2011).

[19] J. Sticht, K.-H. Höck, and J. Kübler, J. Phys.: Cond. Matt. **1**, 8155 (1989).

[20] G. Zimmer and E. Krén, in *Magnetism and Magnetic Materials — 1971 Parts 1 and 2*, edited by C. D. Graham and J. J. Rhyne, AIP Conf. Proc. No. 5 (AIP, New York, 1972).

[21] G. Kádár and E. Krén, Int. J. Magn. **1**, 143 (1971).

[22] S. H. Vosko, L. Wilk, and M. Nusair, Can. J. Phys. **58**, 1200 (1980).

[23] R. Drautz and M. Fähnle, Phys. Rev. B **69**, 104404 (2004).

[24] R. Drautz and M. Fähnle, Phys. Rev. B **72**, 212405 (2005).

[25] B. L. Györffy, A. J. Pindor, J. B. Staunton, G. M. Stocks, and H. Winter, J. Phys. F: Met. Phys. **15**, 1337 (1985).

[26] J. B. Staunton, S. Ostanin, S. S. A. Razee, B. L. Györffy, L. Szunyogh, B. Ginatempo, and E. Bruno, Phys. Rev. Lett. **93**, 257204 (2004).

[27] J. B. Staunton, L. Szunyogh, Á. Buruzs, B. L. Györffy, S. Ostanin, and L. Udvardi, Phys. Rev. B **74**, 144411 (2006).

[28] L. Szunyogh, B. Lazarovits, L. Udvardi, J. Jackson, and U. Nowak, Phys. Rev. B **79**, 020403(R) (2009).

[29] G. Kresse and J. Furthmüller, Phys. Rev. B **54**, 11169 (1996).

[30] J. P. Perdew, K. Burke, and M. Ernzerhof, Phys. Rev. Lett. **77**, 3865 (1996).

[31] J. W. Cable, N. Wakabayashi, and P. Radhakrishna, Solid State Commun. **88**, 161 (1993).

[32] T. Takeda, Z. Physik B **32**, 43 (1978).

[33] H. Ebert, H. Freyer, A. Vernes, and G.-Y. Guo, Phys. Rev. B **53**, 7721 (1996).